

---

# Accelerating Diffusion Models for Inverse Problems through Shortcut Sampling

---

Gongye Liu, Haoze Sun, Jiayi Li, Fei Yin, Yujiu Yang  
Shenzhen International Graduate School, Tsinghua University  
{lgy22, shz22, lijy20, yinf20}@mails.tsinghua.edu.cn,  
yang.yujiu@sz.tsinghua.edu.cn

## Abstract

Recently, diffusion models have demonstrated a remarkable ability to solve inverse problems in an unsupervised manner. Existing methods mainly focus on modifying the posterior sampling process while neglecting the potential of the forward process. In this work, we propose **Shortcut Sampling for Diffusion (SSD)**, a novel pipeline for solving inverse problems. Instead of initiating from random noise, the key concept of SSD is to find the "Embryo", a transitional state that bridges the measurement image  $y$  and the restored image  $x$ . By utilizing the "shortcut" path of "input-Embryo-output", SSD can achieve precise and fast restoration. To obtain the Embryo in the forward process, We propose Distortion Adaptive Inversion (DA Inversion). Moreover, we apply back projection and attention injection as additional consistency constraints during the generation process. Experimentally, we demonstrate the effectiveness of SSD on several representative tasks, including super-resolution, deblurring, and colorization. Compared to state-of-the-art zero-shot methods, our method achieves competitive results with only 30 NFEs. Moreover, SSD with 100 NFEs can outperform state-of-the-art zero-shot methods in certain tasks. Our code is available at [here](#).

## 1 Introduction

Inverse problems are a classic problem in the field of machine learning. Given a low-quality (LQ) input measurement image  $y$  and forward degradation operators  $H$ , inverse problems aim to restore the original high-quality (HQ) image  $x$  from  $y = Hx + n$ . Many image restoration tasks, including super-resolution [9, 35], colorization [19], inpainting [40], deblurring [8, 41] and denoising [37], can be considered as applications of solving inverse problems. In general, the restored image should exhibit two critical attributes: *Realism* and *Faithfulness*. The former indicates that the restored image should be of high-quality and photo-realistic, while the latter denotes that the restored image should be consistent with the input image in the degenerate subspace.

Recently, diffusion models [28, 12, 31] have demonstrated phenomenal performance in generation tasks [26, 7, 39]. Due to their powerful capability in modeling complex distributions, recent methods [16, 15, 5, 3, 36, 20, 30] have sought to utilize pre-trained diffusion models for solving inverse problems in an unsupervised manner. These methods leverage the generative priors of pre-trained models to enhance *realism*, and enforce additional consistency constraints to ensure *faithfulness*.

Despite the successful application of existing methods in solving various inverse problems, their relatively slow sampling speed is a major drawback. Diffusion models have predefined a forward process and a generation process. Existing methods primarily concentrate on the posterior sampling  $p(x|z, y)$  during the generation process while largely ignoring the potential sampling  $p(z|y)$  during the forward process. Instead, these methods typically sample  $z$  directly from the Gaussian prior  $p(z)$ . However, since the initial state of pure noise carries no information about the input LQ image, these

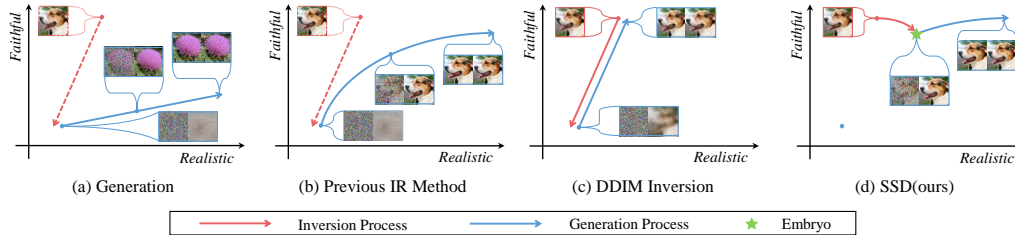


Figure 1: **Visual schematic of different framework.** (a) *Generation* starts from random noise and generates realistic but unfaithful results; (b) *Previous IR methods* modify posterior sampling during the generation process to generate realistic and faithful results; (c) *DDIM Inversion* employs a deterministic inversion process to obtain the "Embryo", achieving faithful but unrealistic reconstruction. (d) *SSD(ours)* adopts a shortcut-sampling strategy by obtaining the "Embryo" through DA Inversion, which generates realistic and faithful results with fewer steps.

methods usually require at least 100-250 neural function evaluations (NFEs) to generate satisfactory results [16, 5, 3, 36, 20].

In this work, we propose **Shortcut Sampling for Diffusion (SSD)**, a novel pipeline for solving inverse problems in a zero-shot manner. The primary concept behind SSD is to find an appropriate transitional state, termed the "**Embryo**", that bridges the gap between the measurement image  $y$  and the restored image  $x$ . By employing a "shortcut" path from the measurement image  $y$  to the Embryo and subsequently to the restored image  $x$ , SSD enables precise and fast restoration.

The Embryo should satisfy the following criterion: (i) It should contain content information from the input image to facilitate the generation process; (ii) It should adhere to the noise distribution prescribed by the diffusion models to retain the capacity for generating a high-quality image. For convenience, we denote the transition from the measurement image  $y$  to the Embryo as the "inversion process" and the transition from the Embryo to the restored image  $x$  as the "generation process".

For the inversion process, the Embryo derived from a random inversion process is random Gaussian noise, lacking any information from the input image. Conversely, employing a deterministic process, such as DDIM Inversion, for obtaining the Embryo can lead to deviations from the predetermined noise distribution, resulting in unrealistic outcomes as illustrated in 1 (c). To address this dilemma, we introduce **Distortion Adaptive Inversion (DA Inversion)**. By adding a controllable random disturbance at each inversion step, DA Inversion is capable of obtaining an Embryo that adheres to the predetermined noise distribution while preserving the majority of the input image.

For the generation process, we introduce back projection tricks[32] as additional consistency constraints. More specifically, we add a projection step after each denoising step to project the image onto the degenerate subspace, thus ensuring consistency. Additionally, we inject the attention map from the inversion process into the generation process to preserve the layout information.

To verify the effectiveness of SSD, we conduct experiments on various inverse problems, including super-resolution, colorization and deblurring on CelebA [13] and ImageNet [6] validation images. Experiments demonstrate that SSD achieves competitive results when compared to state-of-the-art zero-shot methods (with 100 NFEs), despite utilizing only 30 NFEs. Moreover, we find that SSD with 100 NFEs can surpass state-of-the-art methods in certain IR tasks.

## 2 Related Works

### 2.1 Diffusion Models

**Denosing Diffusion Probabilistic Models** Diffusion models [28, 12, 31] are a family of generative models that are used to model complex probability distributions of high-dimensional data. Denosing Diffusion Probabilistic Models(DDPM) [12] comprise both a forward process and a generation process. In the forward process, an image  $x_0$  is transformed into Gaussian noise  $x_T \sim \mathcal{N}(0, 1)$  by gradually adding random noise over  $T$  steps. We can describe each step in the forward process as:

$$x_t = \sqrt{1 - \beta_t}x_{t-1} + \sqrt{\beta_t}\epsilon, \epsilon \sim \mathcal{N}(0, 1) \quad (1)$$

where  $x_{t=0}^T$  is the noisy image at time-step  $t$ ,  $\beta_{t=0}^T$  is the predefined variance schedule. Using reparameterization tricks [18], The resulting noisy image  $x_t$  can be expressed as:

$$x_t = \sqrt{\alpha_t}x_0 + \sqrt{1 - \alpha_t}\bar{\epsilon}_t, \bar{\epsilon}_t \sim \mathcal{N}(0, 1) \quad (2)$$

where  $\alpha_t = \prod_{i=1}^t (1 - \beta_i)$ . The generation process transforms gaussian noise  $x_T$  to image  $x_0$ , the transition from  $x_t$  to  $x_{t-1}$  can be expressed as:

$$x_{t-1} = \frac{1}{\sqrt{1 - \beta_t}}(x_t - \frac{\beta_t}{\sqrt{1 - \alpha_t}}\epsilon_\theta(x_t, t)) + \frac{1 - \alpha_{t-1}}{1 - \alpha_t}\beta_t \quad (3)$$

and  $\epsilon_\theta(x_t, t)$  is a neural network trained to predict the noise  $\epsilon$  from noisy image  $x_t$  at time-step  $t$ . The noise approximation model  $\epsilon_\theta(x_t, t)$  can be trained by minimize the following objective:

$$\min_{\theta} \mathbb{E}_{x_0 \sim q(x_0), \epsilon \sim N(0, I)} \|\epsilon - \epsilon_\theta(x_t, t)\|_2^2 \quad (4)$$

**Denoising Diffusion Implicit Models** DDPM can be regarded as a discrete Stochastic Differential Equations (SDE) which diffuses the data distribution into a fixed Gaussian prior distribution, and the noise approximation model  $\epsilon_\theta(x_t, t)$  is the score function[31]. Meanwhile, DDIM [29] proposed a non-Markov process that shares the same forward process as DDPM, while possessing a deterministic generation process, outlined as follows:

$$x_{t-1} = \sqrt{\alpha_{t-1}}f_\theta(x_t, t) + \sqrt{1 - \alpha_{t-1}}\epsilon_\theta(x_t, t) \quad (5)$$

where  $f_\theta(x_t, t)$  is the prediction of clean image  $x_0$  at time-step  $t$ :

$$f_\theta(x_t, t) = \frac{x_t - \sqrt{1 - \alpha_t}\epsilon_\theta(x_t, t)}{\sqrt{\alpha_t}} \quad (6)$$

## 2.2 Solving an inverse problem in a zero-shot way

Traditional Image Restoration methods typically train an end-to-end model to learn the posterior  $p(x|y)$  for specific tasks. While end-to-end methods can effectively restore images with in-domain degradation, they usually yield poor performance when in the face of out-of-domain degradation. Meanwhile, some methods investigate leveraging the generative priors of pre-trained generative models to restore degraded images in a zero-shot way. GAN Inversion aims to find the closest latent vector in the GAN space for an input image[38, 34, 25, 22]. Using the GAN Inversion technique, PULSE[22] iteratively optimizes the latent code of pre-trained StyleGAN[14] until the output images are consistent with the input image.

**Gradient Guidance** Compared with GAN, Diffusion Models offer a forward process that enables the direct acquisition of latent vectors within the Gaussian noise space. By performing generation processes starting from Gaussian noise and using consistency constraints at each step, diffusion models can be applied to various IR problems, such as super-resolution, inpainting, denoising, and colorization. The purpose of the consistency constraints is to ensure the coherence between  $Hx_{pred}$  and  $y$ . Some methods [15, 1, 5, 3] use the manifold-constrained gradient to make the current noisy image  $x_t$  closer to the manifold, which can be expressed as follows:

$$x'_{t-1} = x_{t-1} - \alpha \frac{\partial}{\partial x_t} \|y - H\hat{x}_0\|_2^2 \quad (7)$$

**Back Projection** Meanwhile, some other methods [5, 36]use back-projection tricks[32] to force the restored image in consistency with the degraded image in the degradation space. The back-projection step can be expressed as follows:

$$x' = (I - H^\dagger H)x + H^\dagger y \quad (8)$$

## 3 Method

As discussed above, diffusion models comprise two processes: a forward process which progressively adds noise to the image to complete Gaussian noise and a generation process which generates realistic

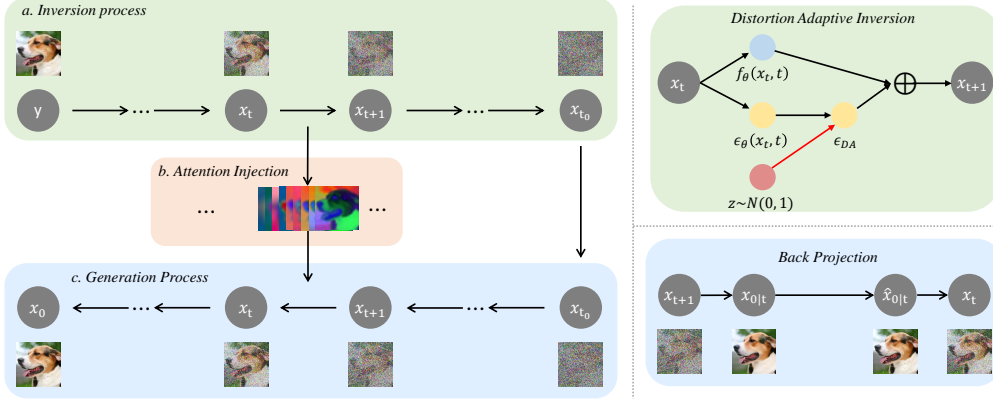


Figure 2: Overview of the proposed SSD

images through iteratively denoising. Previous methods mainly focus on modifying the posterior sampling process  $p(x|z, y)$  during the generation process, while ignoring the utilization of the forward process. Instead, these methods typically sample  $z$  directly from the Gaussian prior  $p(z)$ .

In this work, we propose Shortcut Sampling for Diffusion (SSD), a novel pipeline for solving inverse problems in a zero-shot manner. Different from previous methods that initiate from pure noise, SSD enhances the forward process to obtain an intermediate state called the Embryo, which serves as a bridge between the measurement image  $y$  and the restored image  $x$ . Throughout the shortcut sample path of "input-Embryo-output", SSD can achieve efficient and satisfactory restoration results.

Firstly, we introduce Distortion Adaptive Inversion (DA Inversion) to derive the Embryo from the input LQ image in the inversion process (Sec. 3.1). Subsequently, during the generation process, we iteratively perform the denoising step and the back projection step to generate both faithful and realistic results (Sec. 3.2). Finally, in order to preserve the layout information and further ensure consistency, we inject the attention map obtained from the inversion process into the generation process (Sec. 3.2). The overall pipeline of SSD is illustrated in Fig. 2.

### 3.1 Distortion Adaptive Inversion

We expect to obtain the Embryo by enhancing the forward process. For convenience, we refer to this enhanced forward process as the inversion process. As previously mentioned in Sec. 1, the Embryo should: **(i)** contain content information from the input image; **(ii)** retain the capacity for generating a high-quality image.

**DDIM Inversion** To satisfy **Criterion (i)**, a naive approach is to build a deterministic mapping from the input image  $y$  to the Embryo. Given the deterministic nature of the DDIM generation process, we can establish the DDIM Inversion process by reversing Eq. (5) in the following manner:

$$x_{t+1} = \sqrt{\alpha_{t+1}}f_{\theta}(x_t, t) + \sqrt{1 - \alpha_{t+1}}\epsilon_{\theta}(x_t, t) \quad (9)$$

The Embryo obtained through DDIM Inversion preserves most information of the input images, since we can reconstruct it by iteratively executing Eq. (5). However, as depicted in Fig. 3 (a), the application of this Embryo in the generation process produces faithful but unrealistic results, thus violating **Criterion (ii)**.

We attribute the failure to the observation that, the obtained Embryo deviates from the predefined noise distribution. More specifically, given a low-quality input image  $y$ , the predicted noise  $\{\epsilon_{\theta}(x_t, t)\}$  during DDIM Inversion process deviates from the standard normal distribution, resulting in the deviation of the Embryo from the predefined noise distribution. And during the generation process, the pre-trained model receives out-of-domain input distributions, thereby generating unrealistic results. Further analysis and empirical observations are provided in the appendix to substantiate our assumption.

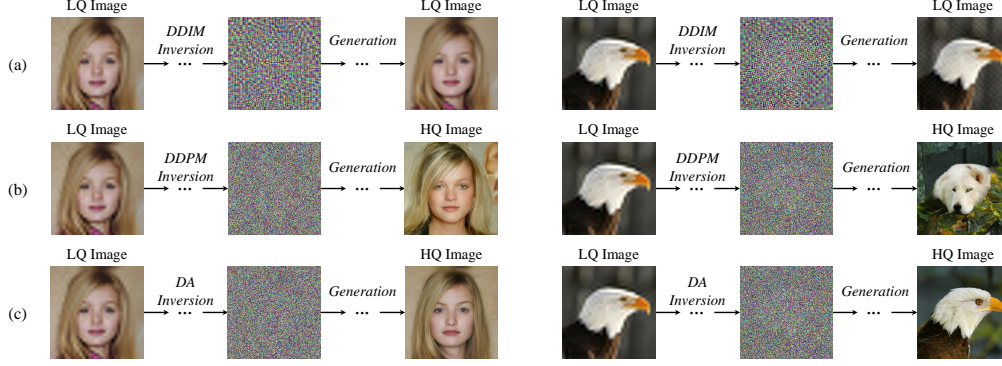


Figure 3: **Comparison of reconstruction results between different Inversion Methods.** (a) *DDIM Inversion* produces faithful but unrealistic results. (b) *DDPM Inversion* produces realistic but unfaithful results (c) *Distortion Adaptive Inversion(ours)* produces both realistic and faithful results

**DDPM Inversion** Based on the above observation, we can improve the realism of reconstruction results by bringing the predicted noise closer to the standard normal distribution. Here we explore an extreme scenario where the predicted noise is replacing with randomly sampled noise from Gaussian distribution. This scenario aligns with the DDPM forward process described in 2. This approach can be regarded as a special inversion technique termed **DDPM Inversion**. Furthermore, we can define it in a similar form of DDIM Inversion as illustrated in 9:

$$x_{t+1} = \sqrt{\alpha_{t+1}}f_{\theta}(x_t, t) + \sqrt{1 - \alpha_{t+1} - \beta_{t+1}}\epsilon_{\theta}(x_t, t) + \sqrt{\beta_{t+1}}z, z \sim \mathcal{N}(0, 1) \quad (10)$$

As shown in Fig. 3(b), DDPM Inversion converts the input image  $y$  into pure noise, thereby violating **Criterion (i)** and producing results that are realistic but lack faithfulness.

**Distortion Adaptive Inversion** Since a deterministic inversion process like DDIM Inversion produces unrealistic results, while a stochastic inversion process like DDPM Inversion yields unfaithful results. To resolve this dilemma, we propose a novel inversion approach called Distortion Adaptive Inversion(DA Inversion). The definition of DA Inversion is as follows:

**Definition 1.** We define the iterative process of Distortion Adaptive Inversion as:

$$x_{t+1} = \sqrt{\alpha_{t+1}}f_{\theta}(x_t, t) + \sqrt{1 - \alpha_{t+1} - \eta\beta_{t+1}}\epsilon_{\theta}(x_t, t) + \sqrt{\eta\beta_{t+1}}z \quad (11)$$

where  $\eta$  control the proportion of random disturbances and  $0 < \eta < 1$ .

For ease of exposition, the predicted noise in DA Inversion at each time-step can be rephrased as:

$$\epsilon_{DA} = \frac{1}{\sqrt{1 - \alpha_{t+1}}}(\sqrt{1 - \alpha_{t+1} - \eta\beta_{t+1}}\epsilon_{\theta}(x_t, t) + \sqrt{\eta\beta_{t+1}}z), z \sim \mathcal{N}(\mu, \sigma) \quad (12)$$

By adding controllable random perturbations in each inverse step, DA Inversion has the capability to generate high-quality images while preserving the essential content, which is shown in Fig. 3 (c).

For **Criterion (i)**, since the random perturbation only replaces a portion of the predicted noise, the Embryo obtained through DA Inversion actually preserves a substantial amount of information from the input image. For **Criterion (ii)**, we have proved that incorporating random disturbances can bring the predicted noise closer to the standard normal distribution  $\mathcal{N}(0, 1)$ .

**Proposition 1.** Assuming  $\epsilon_{\theta}(x_t, t) \sim \mathcal{N}(\mu, \sigma^2)$ , We have:

$$\epsilon_{DA} \sim \mathcal{N}\left(\frac{\sqrt{1 - \alpha_{t+1} - \eta\beta_{t+1}}}{\sqrt{1 - \alpha_{t+1}}}\mu, 1 + \frac{1 - \alpha_{t+1} - \eta\beta_{t+1}}{1 - \alpha_{t+1}}(\sigma^2 - 1)\right) \quad (13)$$

thus:

$$\begin{aligned} \|\mu_{\epsilon_{DA}}\| &< \|\mu\| \\ \|\sigma_{\epsilon_{DA}}^2 - 1\| &< \|\sigma^2 - 1\| \end{aligned} \quad (14)$$

which indicates that after adding random disturbance,  $\epsilon_{DA}$  becomes closer to the standard normal distribution  $z \sim \mathcal{N}(0, 1)$ .

In practice, rather than performing the Inversion process until the last time-step  $T$ , we find that we can achieve acceleration by performing until time-step  $t_0 < T$ , which is inspired by [21, 17, 4].

### 3.2 Back Projection

Although the Embryo obtained from DA Inversion carries information about the input image, and the generation process started from which can produce images with high quality, the result may not entirely align with the input LQ image in the degenerate subspace. To address this problem, we introduce back projection technique in Eq. 8 as consistency constraints during the generation process, which has been discussed in Sec. 3.2.

For details, given an HQ image  $x$ , we can decompose it into two components: the range-space part  $HH^\dagger x$  and the null-space part  $(I - H^\dagger H)x$ . The former ensures that  $x'$  in consistency with LQ image  $y$  in the degenerate subspace  $\{H\mathbb{R}^n = y\}$ , while the latter serves as a supplementary term to account for the lost information during projection. By employing back projection in Eq. 8, we have:

$$Hx' \equiv H[(I - H^\dagger H)x + H^\dagger y] \equiv y \quad (15)$$

which indicates that  $x'$  entirely aligns with the input LQ image  $y$  in the degenerate subspace.

In this work, we employ the back projection step during the generation process. At each time-step, we perform projection after getting predicted  $x_{0|t}$  in (6). Subsequently, in the denoising step of Eq. 5 we substitute  $f_\theta(x_t, t)$  with  $\hat{x}_{0|t}$ , which can be expressed as follows:

$$\hat{x}_{0|t} = (I - H^\dagger H)x_{0|t} + H^\dagger y \quad (16)$$

### 3.3 Attention Injection

Recent large generative models [12, 23, 26] incorporate self-attention layers within the U-Net architecture [24, 27] to enhance the capabilities of the denoising network  $\epsilon_\theta$ . The self-attention computation is performed as follows:

$$\begin{aligned} \text{Attention}(Q, K, V) &= M \cdot V \\ &= \text{Softmax}\left(\frac{QK^T}{\sqrt{d}}\right) \cdot V \end{aligned} \quad (17)$$

Previous studies [10, 33] have demonstrated that there is a strong correlation between the self-attention map and the mutual information of spatial features. By substituting the self-attention maps  $M$ , it is possible to preserve the layout details of the corresponding image.

Based on the above observations, we introduce attention injection to further enhance the faithfulness of restored images. We first preserve the self-attention map  $M_i^t$  during the inversion process at certain time-steps. Then we perform injection of  $M_i^t$  by replacing the original attention map at corresponding time-steps. Importantly, the injection operation hardly incurs additional computational costs. In practice, we only perform attention operations at specific time steps, particularly in the early stages of the generation process when the image layout has not yet been determined.

## 4 Experiments

### 4.1 Experimental Setup

**Pretrained Models and Datasets** To evaluate the performance of SSD, we conduct experiments on two datasets with different distribution characters: CelebA 256×256 [13] for face images and ImageNet 256×256 [6] for natural images, both containing 1k validation images independent of the training dataset. For CelebA 256×256, we use the denoising network VE-SDE[31, 21], which is pre-trained on CelebA<sup>1</sup>. For ImageNet 256×256, we use the denoising network guided-diffusion [7], which is pre-trained on ImageNet<sup>2</sup>.

<sup>1</sup>Pre-trained Model files can be downloaded here provided by SDEdit

<sup>2</sup>Pre-trained Model files can be downloaded here provided by guided-diffusion

CelebA		SR $\times$ 4	SR $\times$ 8	Colorization	Deblur (gauss)	NFEs $\downarrow$
Method	PSNR $\uparrow$ / FID $\downarrow$ / LPIPS $\downarrow$	PSNR $\uparrow$ / FID $\downarrow$ / LPIPS $\downarrow$	FID $\downarrow$ / LPIPS $\downarrow$	PSNR $\uparrow$ / FID $\downarrow$ / LPIPS $\downarrow$	NFEs $\downarrow$	
$H^\dagger y$	28.02 / 128.22 / 0.301	24.77 / 153.86 / 0.460	43.99 / 0.197	19.96 / 116.28 / 0.564	0	
DDRM-30[15]	28.62 / 46.72 / 0.221	26.28 / 49.32 / 0.281	27.69 / 0.214	36.05 / 15.71 / 0.122	<b>30</b>	
DDRM-100[15]	28.84 / 40.52 / 0.214	<u>26.47</u> / 45.22 / 0.273	25.88 / 0.156	36.17 / 15.32 / 0.119	100	
DPS[3]	24.71 / <u>34.69</u> / 0.304	22.38 / <b>41.01</b> / 0.348	N/A	24.89 / 32.64 / 0.288	250	
DDNM[36]	<b>28.85</b> / 35.13 / <u>0.206</u>	<b>26.53</b> / 44.22 / 0.272	<u>23.65</u> / <u>0.138</u>	<b>38.70</b> / <u>4.48</u> / <b>0.062</b>	100	
<b>SSD-30</b>	28.71 / 36.77 / 0.208	26.32 / 44.97 / <u>0.271</u>	24.11 / 0.159	38.34 / 4.98 / 0.065	<b>30</b>	
<b>SSD-100</b>	<b>28.85</b> / <b>32.45</b> / <b>0.202</b>	26.44 / <u>42.42</u> / <b>0.267</b>	<b>23.62</b> / <b>0.138</b>	<u>38.62</u> / <b>4.36</b> / <u>0.060</u>	100	

ImageNet		SR $\times$ 4	SR $\times$ 8	Colorization	Deblur (gauss)	NFEs $\downarrow$
Method	PSNR $\uparrow$ / FID $\downarrow$ / LPIPS $\downarrow$	PSNR $\uparrow$ / FID $\downarrow$ / LPIPS $\downarrow$	FID $\downarrow$ / LPIPS $\downarrow$	PSNR $\uparrow$ / FID $\downarrow$ / LPIPS $\downarrow$	NFEs $\downarrow$	
$H^\dagger y$	26.26 / 106.01 / 0.322	22.86 / 124.89 / 0.4690	27.40 / 0.231	19.33 / 102.33 / 0.553	0	
DDRM-30[15]	27.17 / 46.14 / 0.269	23.50 / 84.53 / 0.426	36.48 / 0.237	35.90 / 13.35 / 0.130	<b>30</b>	
DDRM-100[15]	27.40 / 43.27 / 0.260	23.74 / 83.08 / 0.420	36.44 / 0.224	36.48 / 11.81 / 0.121	100	
DPS[3]	20.34 / 72.33 / 0.485	18.38 / 76.89 / 0.538	N/A	24.89 / 32.64 / 0.288	250	
DDNM[36]	<u>27.44</u> / 39.42 / 0.251	<b>23.80</b> / 80.09 / 0.412	36.46 / <u>0.219</u>	<b>40.48</b> / <u>3.33</u> / <u>0.041</u>	100	
<b>SSD-30</b>	27.13 / <u>38.24</u> / <u>0.251</u>	23.44 / <b>76.35</b> / <u>0.411</u>	<u>36.22</u> / 0.223	39.23 / 4.64 / 0.053	<b>30</b>	
<b>SSD-100</b>	<b>27.45</b> / <b>37.71</b> / <b>0.247</b>	<u>23.76</u> / 82.11 / <b>0.409</b>	<b>35.40</b> / <b>0.215</b>	<u>40.32</u> / <b>3.07</b> / <b>0.039</b>	100	

Table 1: Quantitative evaluation on the **CelebA**(*bottom*) and **ImageNet**(*top*) datasets for various typical IR tasks. **Red** and **blue** indicates the best and second best performance.

**Degradation Operators** We conduct experiments on four typical IR tasks, including Super-Resolution( $\times 4$ ), Super-Resolution( $\times 8$ ), Colorization and Deblurring. The degradation operators are set as follows: (i) For super-resolution, we use a bicubic filter to downsample the image at a given specific scale. (ii) For colorization, we calculate the average value of the red, green and blue channels of the original image to obtain the grayscale image. (iii) For deblurring, we select a Gaussian blur kernel with size  $9 \times 9$  as the blur kernel, and the width is set to  $\sigma = 15.0$ . More details including the specific forms of degradation operator  $H$  can be found in Appendix.

**Evaluation** We use peak signal-to-noise-ratio(PSNR), Frechet Inception Distance(FID)[11], and Learned Perceptual Image Patch Similarity(LPIPS)[42] as the main metrics to quantitatively evaluate the performance of image restoration. Especially due to the inability of PSNR to capture colorization performance, we use FID and LPIPS for colorization. Additionally, we use Neural Function Evaluations(NFEs) as the metrics of sampling speed, which is a commonly employed benchmark in diffusion model-based methods. Since SSD introduces an additional inversion process, the NFEs of SSD are calculated by summing the steps involved in both the inversion process and the generation process.

**Comparison Methods** We compare the restoration performance of the proposed method with recent State-Of-The-Art zero-shot image restoration methods using pre-trained diffusion models: DDRM[15], DPS[3] and DDNM[36]. DDRM is well known for better performance in low NFEs. DPS achieves SOTA performance in gradient-guided-based methods. And DDNM achieves SOTA performance in back-projection-based methods. For a fair comparison, all methods above use the same pre-trained denoising networks and the same degradation operator.

## 4.2 Results

We compare SSD (with 30 and 100 steps) with previous methods mentioned in Sec 4.1. The quantitative evaluation results shown in Table 1 illustrate that the proposed method achieves competitive results compared to state-of-the-art methods. When setting NFE to 30, SSD-30 outperforms other methods known for fast sampling like DDRM-30 and achieves better perception-oriented metrics (i.e., FID, LPIPS) than SOTA methods (DDNM with 100 NFEs). When setting NFE to 100, SSD-100 achieves SOTA performance in many IR tasks, including SR  $\times 4$  and colorization. As shown in Fig. 4, 5, SSD generates high-quality restoration results in all tested datasets and tasks.



Figure 4: Qualitative results of different zero-shot IR methods on CelebA and Imagenet Dataset.

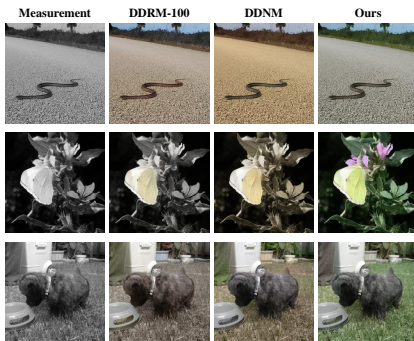


Figure 5: Colorization results of different zero-shot IR methods on ImageNet Dataset

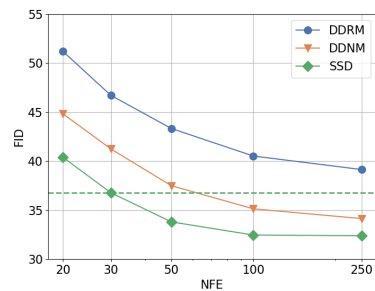


Figure 6: Comparison of the performance of various methods affected by NFEs with  $SR \times 4$  task on CelebA dataset

We further explore the performance of various methods in terms of FID with respect to the change in NFEs, which is shown in Fig. 6. We conduct experiments with  $SR \times 4$  task on the CelebA dataset. Results show that SSD outperforms all the other methods in both high NFEs and low NFEs and does not exhibit significant performance degradation as NFE decreases.

### 4.3 Ablation Study

**Faithfulness-Realism Trade-off** We investigate the performance of the proposed DA Inversion by exploring the effects of different parameters. While SSD achieves competitive results under various

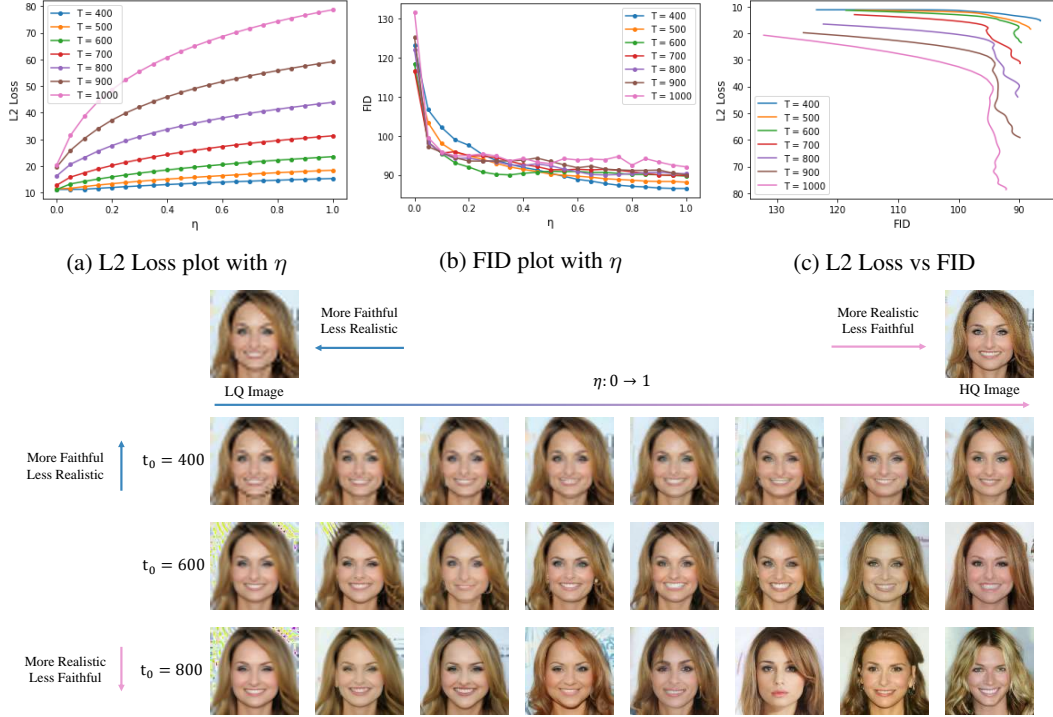


Figure 7: The Faithfulness-Realism trade-off affected by  $\eta$  and  $t_0$ .

parameters, the generation results of DA Inversion **alone** exhibit a noticeable trade-off between realism and faithfulness when choosing different values of  $(t_0, \lambda)$ .

To further illustrate it, we randomly select 100 images from the Celeba-Test Dataset and apply 4 $\times$  average-pooling downsampler on them as the input LQ Images. We then perform DA inversion with various  $(t_0, \lambda)$  values and proceed with the generation process. For *faithfulness*, we compute the average  $L_2$  distance between the generation results and the input LQ Images. For *realism*, we use FID to quantify the distribution difference. Fig. 7 illustrates the trade-off where faithfulness decreases and realism increases as  $\eta$  increases. Notably, this trade-off follows an upward convex curve in 7c, suggesting that we can achieve a combination of faithfulness and realism by appropriately selecting hyperparameters.

## 5 Conclusion and Discussion

In this paper, we propose SSD, a novel framework for solving inverse problems in a zero-shot manner. SSD can achieve acceleration of the sampling process through the "LQ-Embryo-HQ" *shortcut*. We also empirically analyze why the proposed DA inversion can generate both faithful and realistic results compared to other inversion process. Experimentally, we demonstrate the effectiveness of SSD on various IR tasks, including super-resolution, colorization, and deblurring. Compared to SOTA methods, SSD can achieve competitive results with only 30 NFEs, and can outperform SOTA methods with 100 NFEs in certain tasks.

**Limitations** The proposed SSD mainly focuses on non-blind linear inverse problems, relying on a known degradation operator. which may be challenging to obtain in real-world scenarios where the degradation operator. One possible solution is to introduce additional supervised information and design a special module to estimate the unknown degradation operator[2]. Designing methods that can effectively apply to unknown degradation, especially real-world degradation, may be a promising research direction.

## References

- [1] Jooyoung Choi, Sungwon Kim, Yonghyun Jeong, Youngjune Gwon, and Sungroh Yoon. ILVR: Conditioning method for denoising diffusion probabilistic models. In *Proceedings of the IEEE/CVF International Conference on Computer Vision (ICCV)*, 2021.
- [2] Hyungjin Chung, Jeongsol Kim, Sehui Kim, and Jong Chul Ye. Parallel diffusion models of operator and image for blind inverse problems. In *Proceedings of the IEEE/CVF Conference on Computer Vision and Pattern Recognition*, 2023.
- [3] Hyungjin Chung, Jeongsol Kim, Michael T Mccann, Marc L Klasky, and Jong Chul Ye. Diffusion posterior sampling for general noisy inverse problems. In *International Conference on Learning Representations (ICLR)*, 2023.
- [4] Hyungjin Chung, Byeongsu Sim, and Jong Chul Ye. Come-Closer-Diffuse-Faster: Accelerating Conditional Diffusion Models for Inverse Problems through Stochastic Contraction. In *Proceedings of the IEEE/CVF Conference on Computer Vision and Pattern Recognition*, 2022.
- [5] Hyungjin Chung, Byeongsu Sim, and Jong Chul Ye. Improving diffusion models for inverse problems using manifold constraints. In *Advances in Neural Information Processing Systems (NeurIPS)*, 2022.
- [6] Jia Deng, Wei Dong, Richard Socher, Li-Jia Li, Kai Li, and Li Fei-Fei. Imagenet: A large-scale hierarchical image database. In *2009 IEEE conference on computer vision and pattern recognition*, pages 248–255. Ieee, 2009.
- [7] Prafulla Dhariwal and Alexander Quinn Nichol. Diffusion models beat GANs on image synthesis. In A. Beygelzimer, Y. Dauphin, P. Liang, and J. Wortman Vaughan, editors, *Advances in Neural Information Processing Systems*, 2021.
- [8] Shi Guo, Zifei Yan, Kai Zhang, Wangmeng Zuo, and Lei Zhang. Toward convolutional blind denoising of real photographs. In *Proceedings of the IEEE/CVF conference on computer vision and pattern recognition*, pages 1712–1722, 2019.
- [9] Muhammad Haris, Gregory Shakhnarovich, and Norimichi Ukita. Deep back-projection networks for super-resolution. In *Proceedings of the IEEE conference on computer vision and pattern recognition*, pages 1664–1673, 2018.
- [10] Amir Hertz, Ron Mokady, Jay Tenenbaum, Kfir Aberman, Yael Pritch, and Daniel Cohen-Or. Prompt-to-prompt image editing with cross attention control. *arXiv preprint arXiv:2208.01626*, 2022.
- [11] Martin Heusel, Hubert Ramsauer, Thomas Unterthiner, Bernhard Nessler, and Sepp Hochreiter. Gans trained by a two time-scale update rule converge to a local nash equilibrium. In *Advances in neural information processing systems*, volume 30, 2017.
- [12] Jonathan Ho, Ajay Jain, and Pieter Abbeel. Denoising diffusion probabilistic models. In *Advances in Neural Information Processing Systems*, volume 33, pages 6840–6851, 2020.
- [13] Tero Karras, Timo Aila, Samuli Laine, and Jaakko Lehtinen. Progressive growing of gans for improved quality, stability, and variation. *arXiv preprint arXiv:1710.10196*, 2017.
- [14] Tero Karras, Samuli Laine, and Timo Aila. A style-based generator architecture for generative adversarial networks. In *Proceedings of the IEEE/CVF conference on computer vision and pattern recognition*, pages 4401–4410, 2019.
- [15] Bahjat Kawar, Michael Elad, Stefano Ermon, and Jiaming Song. Denoising diffusion restoration models. In *ICLR Workshop on Deep Generative Models for Highly Structured Data*, 2022.
- [16] Bahjat Kawar, Gregory Vaksman, and Michael Elad. Snips: Solving noisy inverse problems stochastically. *Advances in Neural Information Processing Systems*, 34:21757–21769, 2021.
- [17] Gwanghyun Kim, Taesung Kwon, and Jong Chul Ye. Diffusionclip: Text-guided diffusion models for robust image manipulation. In *Proceedings of the IEEE/CVF Conference on Computer Vision and Pattern Recognition*, pages 2426–2435, 2022.

- [18] Diederik P Kingma and Max Welling. Auto-encoding variational bayes. *arXiv preprint arXiv:1312.6114*, 2013.
- [19] Gustav Larsson, Michael Maire, and Gregory Shakhnarovich. Learning representations for automatic colorization. In *Computer Vision—ECCV 2016: 14th European Conference, Amsterdam, The Netherlands, October 11–14, 2016, Proceedings, Part IV 14*, pages 577–593. Springer, 2016.
- [20] Andreas Lugmayr, Martin Danelljan, Andres Romero, Fisher Yu, Radu Timofte, and Luc Van Gool. Repaint: Inpainting using denoising diffusion probabilistic models. In *Proceedings of the IEEE/CVF Conference on Computer Vision and Pattern Recognition (CVPR)*, pages 11461–11471, June 2022.
- [21] Chenlin Meng, Yang Song, Jiaming Song, Jiajun Wu, Jun-Yan Zhu, and Stefano Ermon. SDEdit: Image synthesis and editing with stochastic differential equations. *arXiv preprint arXiv:2108.01073*, 2021.
- [22] Sachit Menon, Alexandru Damian, Shijia Hu, Nikhil Ravi, and Cynthia Rudin. Pulse: Self-supervised photo upsampling via latent space exploration of generative models. In *Proceedings of the IEEE/CVF conference on computer vision and pattern recognition*, pages 2437–2445, 2020.
- [23] Alexander Quinn Nichol and Prafulla Dhariwal. Improved denoising diffusion probabilistic models. In *International Conference on Machine Learning*, pages 8162–8171. PMLR, 2021.
- [24] Ozan Oktay, Jo Schlemper, Loic Le Folgoc, Matthew Lee, Mattias Heinrich, Kazunari Misawa, Kensaku Mori, Steven McDonagh, Nils Y Hammerla, Bernhard Kainz, et al. Attention u-net: Learning where to look for the pancreas. *arXiv preprint arXiv:1804.03999*, 2018.
- [25] Xingang Pan, Xiaohang Zhan, Bo Dai, Dahua Lin, Chen Change Loy, and Ping Luo. Exploiting deep generative prior for versatile image restoration and manipulation. *IEEE Transactions on Pattern Analysis and Machine Intelligence*, 44(11):7474–7489, 2021.
- [26] Robin Rombach, Andreas Blattmann, Dominik Lorenz, Patrick Esser, and Björn Ommer. High-resolution image synthesis with latent diffusion models. In *Proceedings of the IEEE/CVF Conference on Computer Vision and Pattern Recognition*, pages 10684–10695, 2022.
- [27] Olaf Ronneberger, Philipp Fischer, and Thomas Brox. U-net: Convolutional networks for biomedical image segmentation. In *Medical Image Computing and Computer-Assisted Intervention—MICCAI 2015: 18th International Conference, Munich, Germany, October 5-9, 2015, Proceedings, Part III 18*, pages 234–241. Springer, 2015.
- [28] Jascha Sohl-Dickstein, Eric Weiss, Niru Maheswaranathan, and Surya Ganguli. Deep unsupervised learning using nonequilibrium thermodynamics. In *International Conference on Machine Learning*, pages 2256–2265. PMLR, 2015.
- [29] Jiaming Song, Chenlin Meng, and Stefano Ermon. Denoising diffusion implicit models. In *9th International Conference on Learning Representations, ICLR*, 2021.
- [30] Yang Song, Liyue Shen, Lei Xing, and Stefano Ermon. Solving inverse problems in medical imaging with score-based generative models. In *International Conference on Learning Representations (ICLR)*, 2021.
- [31] Yang Song, Jascha Sohl-Dickstein, Diederik P. Kingma, Abhishek Kumar, Stefano Ermon, and Ben Poole. Score-based generative modeling through stochastic differential equations. In *9th International Conference on Learning Representations, ICLR*, 2021.
- [32] Tom Tirer and Raja Giryes. Image restoration by iterative denoising and backward projections. *IEEE Transactions on Image Processing*, 28(3):1220–1234, 2018.
- [33] Narek Tumanyan, Michal Geyer, Shai Bagon, and Tali Dekel. Plug-and-play diffusion features for text-driven image-to-image translation. In *Proceedings of the IEEE/CVF Conference on Computer Vision and Pattern Recognition (CVPR)*, pages 1921–1930, June 2023.

- [34] Dmitry Ulyanov, Andrea Vedaldi, and Victor Lempitsky. Deep image prior. In *Proceedings of the IEEE conference on computer vision and pattern recognition*, pages 9446–9454, 2018.
- [35] Xintao Wang, Ke Yu, Shixiang Wu, Jinjin Gu, Yihao Liu, Chao Dong, Yu Qiao, and Chen Change Loy. Esrgan: Enhanced super-resolution generative adversarial networks. In *Proceedings of the European conference on computer vision (ECCV) workshops*, pages 0–0, 2018.
- [36] Yinhuai Wang, Jiwen Yu, and Jian Zhang. Zero-shot image restoration using denoising diffusion null-space model. In *International Conference on Learning Representations (ICLR)*, 2023.
- [37] Zhendong Wang, Xiaodong Cun, Jianmin Bao, Wengang Zhou, Jianzhuang Liu, and Houqiang Li. Uformer: A general u-shaped transformer for image restoration. In *Proceedings of the IEEE/CVF Conference on Computer Vision and Pattern Recognition*, pages 17683–17693, 2022.
- [38] Weihao Xia, Yulun Zhang, Yujiu Yang, Jing-Hao Xue, Bolei Zhou, and Ming-Hsuan Yang. Gan inversion: A survey. *IEEE Transactions on Pattern Analysis and Machine Intelligence*, 2022.
- [39] Zhisheng Xiao, Karsten Kreis, and Arash Vahdat. Tackling the generative learning trilemma with denoising diffusion gans. In *Advances in Neural Information Processing Systems (NeurIPS)*, 2022.
- [40] Raymond A Yeh, Chen Chen, Teck Yian Lim, Alexander G Schwing, Mark Hasegawa-Johnson, and Minh N Do. Semantic image inpainting with deep generative models. In *Proceedings of the IEEE conference on computer vision and pattern recognition*, pages 5485–5493, 2017.
- [41] Kai Zhang, Wangmeng Zuo, and Lei Zhang. Ffdnet: Toward a fast and flexible solution for cnn-based image denoising. *IEEE Transactions on Image Processing*, 27(9):4608–4622, 2018.
- [42] Richard Zhang, Phillip Isola, Alexei A Efros, Eli Shechtman, and Oliver Wang. The unreasonable effectiveness of deep features as a perceptual metric. In *Proceedings of the IEEE conference on computer vision and pattern recognition*, pages 586–595, 2018.

## A Proofs

**Definition 1.** We define the iterative process of Distortion Adaptive Inversion as:

$$x_{t+1} = \sqrt{\alpha_{t+1}}f_{\theta}(x_t, t) + \sqrt{1 - \alpha_{t+1} - \eta\beta_{t+1}}\epsilon_{\theta}(x_t, t) + \sqrt{\eta\beta_{t+1}}z \quad (11)$$

where  $\eta$  control the proportion of random disturbances and  $0 < \eta < 1$ .

For ease of exposition, the predicted noise in DA Inversion at each time-step can be rephrased as:

$$\epsilon_{DA} = \frac{1}{\sqrt{1 - \alpha_{t+1}}}(\sqrt{1 - \alpha_{t+1} - \eta\beta_{t+1}}\epsilon_{\theta}(x_t, t) + \sqrt{\eta\beta_{t+1}}z), z \sim \mathcal{N}(\mu, \sigma) \quad (12)$$

**Proposition 1.** Assuming  $\epsilon_{\theta}(x_t, t) \sim \mathcal{N}(\mu, \sigma^2)$ , We have:

$$\epsilon_{DA} \sim \mathcal{N}\left(\frac{\sqrt{1 - \alpha_{t+1} - \eta\beta_{t+1}}}{\sqrt{1 - \alpha_{t+1}}}\mu, 1 + \frac{1 - \alpha_{t+1} - \eta\beta_{t+1}}{1 - \alpha_{t+1}}(\sigma^2 - 1)\right) \quad (13)$$

thus:

$$\begin{aligned} \|\mu_{\epsilon_{DA}}\| &< \|\mu\| \\ \|\sigma_{\epsilon_{DA}}^2 - 1\| &< \|\sigma^2 - 1\| \end{aligned} \quad (14)$$

which indicates that after adding random disturbance,  $\epsilon_{DA}$  becomes closer to the standard normal distribution  $z \sim \mathcal{N}(0, 1)$ .

*Proof.* According to Eq. 12, we can rewrite it based on reparameterization techniques:

$$z_1 = \frac{\sqrt{1 - \alpha_{t+1} - \eta\beta_{t+1}}}{\sqrt{1 - \alpha_{t+1}}}\epsilon_{\theta}(x_t, t) \quad (18)$$

$$z_2 = \frac{\sqrt{\eta\beta_{t+1}}}{\sqrt{1 - \alpha_{t+1}}}z \quad (19)$$

$$\epsilon_{DA} = z_1 + z_2 \quad (20)$$

further:

$$z_1 \sim \mathcal{N}\left(\frac{\sqrt{1 - \alpha_{t+1} - \eta\beta_{t+1}}}{\sqrt{1 - \alpha_{t+1}}}\mu, \frac{1 - \alpha_{t+1} - \eta\beta_{t+1}}{1 - \alpha_{t+1}}\sigma^2\right) \quad (21)$$

$$z_2 \sim \mathcal{N}\left(0, \frac{\eta\beta_{t+1}}{1 - \alpha_{t+1}}\right) \quad (22)$$

Since  $z$  is sampled randomly and independently from the standard normal distribution, it is mutually independent of  $\epsilon_{\theta}(x_t, t)$ . Additionally,  $z_1$  and  $z_2$  are also mutually independent. Therefore we have:

$$\mu_{\epsilon_{DA}} = \mu_{z_1} + \mu_{z_2} \quad (23)$$

$$= \frac{\sqrt{1 - \alpha_{t+1} - \eta\beta_{t+1}}}{\sqrt{1 - \alpha_{t+1}}}\mu \quad (24)$$

$$\sigma_{\epsilon_{DA}}^2 = \sigma_{z_1}^2 + \sigma_{z_2}^2 \quad (25)$$

$$= \frac{1 - \alpha_{t+1} - \eta\beta_{t+1}}{1 - \alpha_{t+1}}\sigma^2 + \frac{\eta\beta_{t+1}}{1 - \alpha_{t+1}} \quad (26)$$

$$= 1 + \frac{1 - \alpha_{t+1} - \eta\beta_{t+1}}{1 - \alpha_{t+1}}(\sigma^2 - 1) \quad (27)$$

thus we have:

$$0 < \|\mu_{\epsilon_{DA}}\| < \|\mu\| \quad (28)$$

$$\begin{cases} 1 < \sigma_{\epsilon_{DA}}^2 < \sigma^2, \sigma^2 > 1 \\ \sigma^2 < \sigma_{\epsilon_{DA}}^2 < 1, \sigma^2 < 1 \end{cases} \quad (29)$$

which indicates that by introducing random disturbance, the mean of  $\epsilon_{DA}$  tends to approach 0 in comparison to the original noise mean  $\mu$ , while the variance of  $\epsilon_{DA}$  tends to approach 1 in comparison to the original noise variance  $\sigma^2$ . As a result,  $\epsilon_{DA}$  exhibits a closer resemblance to the standard normal distribution  $z \sim \mathcal{N}(0, 1)$ . □

## B The Deviation from Standard Normal Distribution during the Inversion Process

We observe that the predicted noise  $\epsilon_{\theta}(x_t, t)$  during DDIM Inversion process deviates from the standard normal distribution. As the diffusion models are pretrained to generate high-quality images from the standard normal distribution, employing out-of-domain input distributions may undermine the generation performance, leading to unrealistic results. We further define this as the following assumption:

**Assumption 1.** *The distribution of predicted noise  $\epsilon_{\theta}(x_t, t)$  during the DDIM Inversion process varies significantly depending on the quality of the input images. The predicted noise of low-quality input images exhibits a greater deviation from the standard normal distribution.*

To provide further illustration, we performed validation experiments on ImageNet dataset. We randomly select 100 images from ImageNet validation dataset and apply DDIM Inversion on input images with varying degrees of degradation, including original high-quality images, as well as images downsampled by factors of 2, 4 and 8 using bicubic interpolation. We utilize the Kullback-Leibler (KL) divergence as a metric to quantify the deviation from the standard normal distribution, given by:

$$D_{KL}(P\|Q) = \int_{-\infty}^{\infty} p(x) \log \left( \frac{p(x)}{q(x)} \right) dx \quad (30)$$

As depicted in Fig. 8, it can be observed that as the downsampling scale increases, the noise in the DDIM inversion process deviates further from the standard normal distribution. In contrast, during the proposed DA Inversion process, the predicted noise approaches the standard normal distribution  $z \sim \mathcal{N}(0, 1)$ . This outcome validates our previous hypothesis stated in Prop. 1.

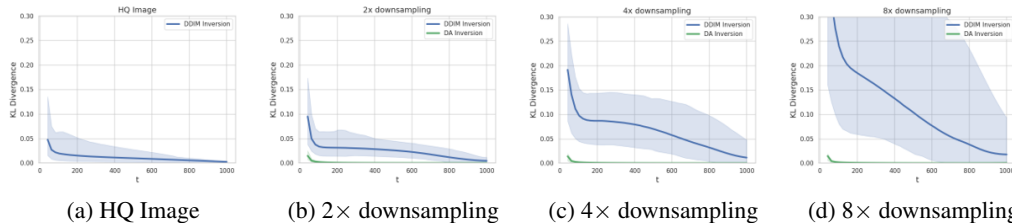


Figure 8: Deviation of noise during the inversion process of differently degraded images. We observe that with the increase in the degree of image degradation, the deviation between the predicted noise and the standard normal distribution also increases. In contrast, the proposed DA Inversion does not exhibit such deviation.

## C Connections between DDIM Inversion, DDPM Inversion, and Distortion Adaptive Inversion

In the main text, we attribute the failure of DDIM Inversion to the deviation from the standard normal distributions. In this section, we further explore the reasons behind the out-of-domain results produced by DDIM Inversion after multiple iterations in the inversion process.

Let's first review the forward process in diffusion models, which can be expressed as follows[12]:

$$x_{t+1} = \sqrt{\alpha_{t+1}}x_0 + \sqrt{1 - \alpha_{t+1}}\bar{\epsilon}_{t+1}, \bar{\epsilon}_{t+1} \sim \mathcal{N}(0, 1) \quad (1)$$

$$x_{t+1} = \sqrt{1 - \beta_{t+1}}x_t + \sqrt{\beta_{t+1}}\epsilon, \epsilon \sim \mathcal{N}(0, 1) \quad (2)$$

And DDIM Inversion process is defined as:

$$x_{t+1} = \sqrt{\alpha_{t+1}}f_{\theta}(x_t, t) + \sqrt{1 - \alpha_{t+1}}\epsilon_{\theta}(x_t, t) \quad (9)$$

Notice that the forward process in Eq. 1 and the DDIM Inversion process in Eq. 9 share a similar form, wherein  $f_{\theta}(x_t, t)$  substitutes  $x_0$  and  $\epsilon_{\theta}(x_t, t)$  replaces the noise  $\bar{\epsilon}_{t+1}$ . It is important to note that  $\epsilon_{\theta}(x_t, t)$  is the approximation of the noise added until time-step  $t$ , and  $\bar{\epsilon}_{t+1}$  represents the noise added until time-step  $t + 1$ . To account for this misalignment, we rewrite Eq. 1 as follows:

$$\begin{aligned} x_{t+1} &= \sqrt{1 - \beta_{t+1}}x_t + \sqrt{\beta_{t+1}}\epsilon_{t+1} \\ &= \sqrt{(1 - \beta_{t+1})(1 - \beta_t)}x_{t-1} + \sqrt{(1 - \beta_{t+1})\beta_t}\epsilon_t + \sqrt{\beta_{t+1}}\epsilon_{t+1} \\ &= \dots \\ &= \sqrt{\alpha_t}x_0 + \sqrt{1 - \alpha_{t+1}}\bar{\epsilon}_{t+1} \end{aligned} \quad (31)$$

where:

$$\begin{aligned} \sqrt{1 - \alpha_{t+1}}\bar{\epsilon}_{t+1} &= \sqrt{\beta_{t+1}}\epsilon_{t+1} + \sqrt{(1 - \beta_{t+1})\beta_t}\epsilon_t + \sqrt{(1 - \beta_{t+1})(1 - \beta_t)}\beta_{t-1}\epsilon_{t-1} \\ &\quad + \dots + \sqrt{(1 - \beta_{t+1})(1 - \beta_t)}\dots(1 - \beta_2)\beta_1\epsilon_1 \\ &= \sqrt{\beta_{t+1}}\epsilon_{t+1} + \sqrt{(1 - \beta_{t+1})\beta_t}\epsilon_t + (1 - \beta_{t+1})(1 - \beta_t)\beta_{t-1} + \dots\bar{\epsilon}_t \\ &= \sqrt{\beta_{t+1}}\epsilon_{t+1} + \sqrt{(1 - \alpha_{t+1}) - \beta_{t+1}}\bar{\epsilon}_t \end{aligned} \quad (32)$$

therefore we have:

$$x_{t+1} = \sqrt{\alpha_{t+1}}x_0 + \underbrace{\sqrt{(1 - \alpha_{t+1}) - \beta_{t+1}}\bar{\epsilon}_t}_{\text{Synthesis of the first } t\text{-term noise}} + \underbrace{\sqrt{\beta_{t+1}}\epsilon_{t+1}}_{\text{the } t + 1 \text{ term noise}} \quad (33)$$

where  $\epsilon_{t+1}$  is independent of  $\bar{\epsilon}_t$ .

During the forward (inversion) process from  $t$  to  $t + 1$ , we can interpret  $\bar{\epsilon}_t$  as the existing information in  $x_t$ , and  $\epsilon_{t+1}$  as the additional information. By setting  $\bar{\epsilon}_t = \epsilon_{\theta}(x_t, t) \sim \mathcal{N}(0, 1)$  and maintain  $\epsilon_{t+1}$  stochastic (where  $\epsilon_{\theta}(x_t, t)$  is independent of  $\epsilon_{t+1}$ ), we can build a fully stochastic process. This is equivalent to the forward process described in Eq. 2, which is referred to as "DDPM Inversion":

$$\begin{aligned}
x_{t+1} &= \sqrt{\alpha_{t+1}}f_{\theta}(x_t, t) + \sqrt{(1 - \alpha_{t+1}) - \beta_{t+1}}\epsilon_{\theta}(x_t, t) + \sqrt{\beta_{t+1}}z \\
&= \sqrt{\alpha_{t+1}}\frac{x_t - \sqrt{1 - \alpha_t}\epsilon_{\theta}(x_t, t)}{\sqrt{\alpha_t}} + \sqrt{(1 - \alpha_{t+1}) - \beta_{t+1}}\epsilon_{\theta}(x_t, t) + \sqrt{\beta_{t+1}}z \\
&= \sqrt{\alpha_{t+1}}x_t - \sqrt{\frac{(1 - \alpha_t)\alpha_{t+1}}{\alpha_t}} + \sqrt{1 - \alpha_{t+1} - \beta_{t+1}}\epsilon_{\theta}(x_t, t) + \sqrt{\beta_{t+1}}z \\
&= \sqrt{\alpha_{t+1}}x_t - \sqrt{\frac{\alpha_{t+1}}{\alpha_t}} - \alpha_{t+1}\epsilon_{\theta}(x_t, t) + \sqrt{1 - \alpha_{t+1} - \beta_{t+1}}\epsilon_{\theta}(x_t, t) + \sqrt{\beta_{t+1}}z \\
&= \sqrt{\alpha_{t+1}}x_t - \sqrt{1 - \alpha_{t+1} - \beta_{t+1}}\epsilon_{\theta}(x_t, t) + \sqrt{1 - \alpha_{t+1} - \beta_{t+1}}\epsilon_{\theta}(x_t, t) + \sqrt{\beta_{t+1}}z \\
&= \sqrt{\alpha_{t+1}}x_t + \sqrt{\beta_{t+1}}z
\end{aligned} \tag{34}$$

Similarly, we can rewrite Eq. 9 as a similar form to Eq. 33, given by:

$$\begin{aligned}
x_{t+1} &= \sqrt{\alpha_{t+1}}x_0 + \underbrace{\sqrt{1 - \alpha_{t+1} - \beta_{t+1}}\epsilon_{\theta}(x_t, t)}_{\text{Synthesis of the first } t\text{-term noise}} + \underbrace{(\sqrt{1 - \alpha_{t+1}} - \sqrt{1 - \alpha_{t+1} - \beta_{t+1}})\epsilon_{\theta}(x_t, t)}_{\text{the } t + 1 \text{ term noise}} \\
&= \sqrt{\alpha_{t+1}}x_t + (\sqrt{1 - \alpha_{t+1}} - \sqrt{1 - \alpha_{t+1} - \beta_{t+1}})\epsilon_{\theta}(x_t, t)
\end{aligned} \tag{35}$$

We adjust the coefficient of the  $t + 1$  term noise because they do not satisfy independence. DDIM Inversion is a deterministic process because the  $t + 1$  term noise inherits the information of  $x_t$ .

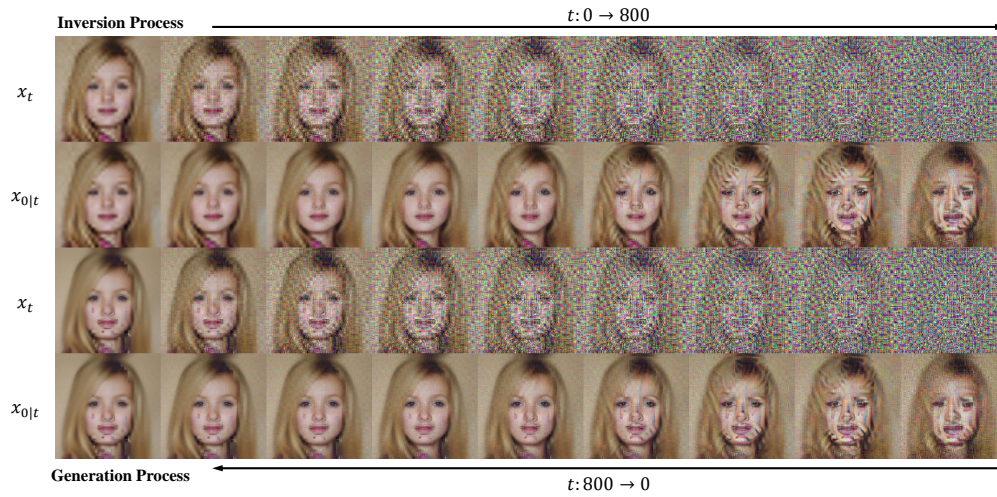
Further, the proposed DA Inversion takes into account both the information inherited from  $x_t$  and additional randomness. The formulation is as follows.

$$\begin{aligned}
x_{t+1} &= \sqrt{\alpha_{t+1}}x_0 + \underbrace{\sqrt{1 - \alpha_{t+1} - \beta_{t+1}}\epsilon_{\theta}(x_t, t)}_{\text{Synthesis of the first } t\text{-term noise}} + \\
&\quad \underbrace{(\sqrt{1 - \alpha_{t+1} - \eta\beta_{t+1}} - \sqrt{1 - \alpha_{t+1} - \beta_{t+1}})\epsilon_{\theta}(x_t, t) + \sqrt{\eta\beta_{t+1}}z}_{\text{the } t + 1 \text{ term noise}} \\
&= \sqrt{\alpha_{t+1}}x_t + (\sqrt{1 - \alpha_{t+1} - \eta\beta_{t+1}} - \sqrt{1 - \alpha_{t+1} - \beta_{t+1}})\epsilon_{\theta}(x_t, t) + \sqrt{\eta\beta_{t+1}}z
\end{aligned} \tag{36}$$

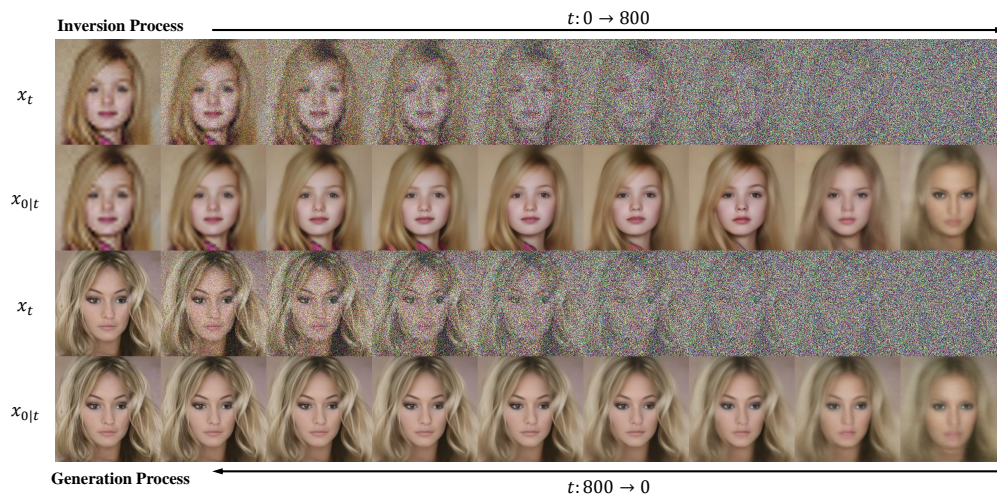
The comparison of different inversion methods, namely DDIM Inversion, DDPM Inversion, and our proposed Distorted Adaptive Inversion, is summarized in Table 2. We also visualize the inversion process of different methods, as shown in Fig. 9 10.

		DDIM Inversion [29]	DDPM Inversion [12]	DA Inversion (ours)
<b>Inversion</b>				
Inversion Process		Equation 9	Equation 33	Equation 11
<b>Composition of <math>t + 1</math> term noise</b>				
Coefficient of $\epsilon_{\theta}(x_t, t)$	$c(\epsilon_{\theta})$	$\sqrt{1 - \alpha_{t+1}}$ $-\sqrt{1 - \alpha_{t+1} - \beta_{t+1}}$	0	$\sqrt{1 - \alpha_{t+1} - \eta\beta_{t+1}}$ $-\sqrt{1 - \alpha_{t+1} - \beta_{t+1}}$
Coefficient of $z$	$c(z)$	0	$\sqrt{\beta_{t+1}}$	$\sqrt{\eta\beta_{t+1}}$
<b>Performance</b>				
Faithfulness		✓	✗	✓
Realism		✗	✓	✓

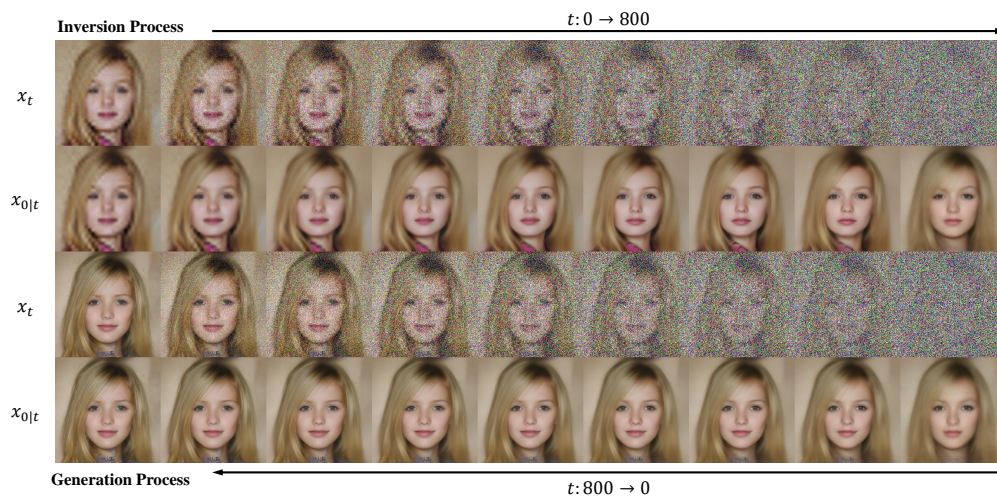
Table 2: Comparisons on different inversion methods.



(a) DDIM Inversion

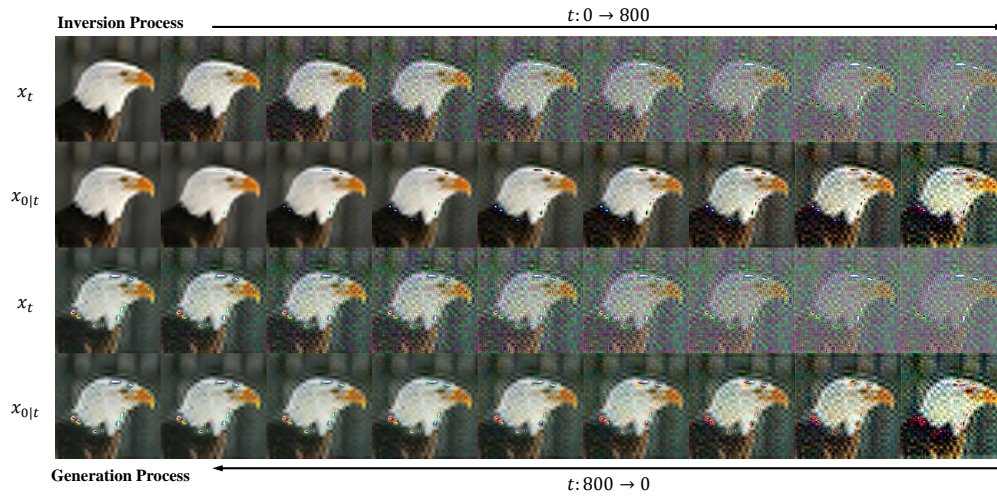


(b) DDPM Inversion

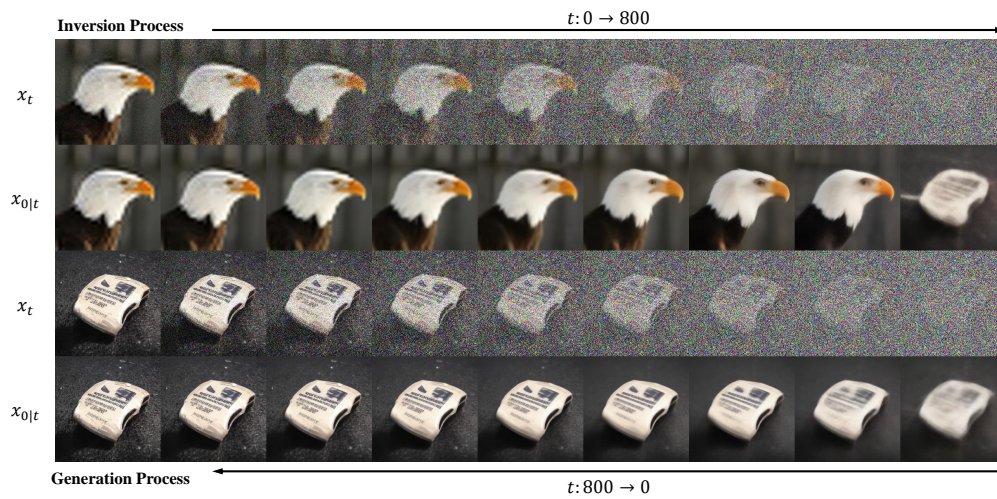


(c) DA Inversion (ours)

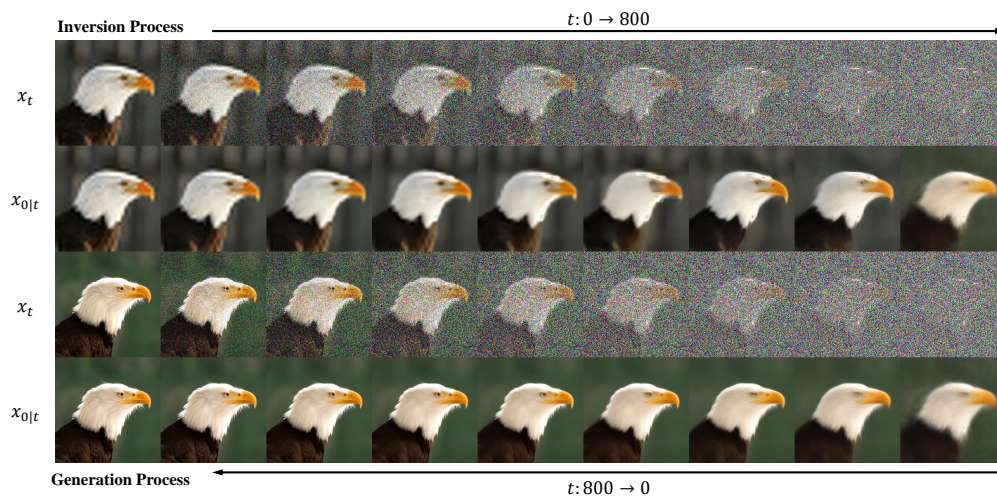
Figure 9: Visualization results of various inversion process on CelebA



(a) DDIM Inversion



(b) DDPM Inversion



(c) DA Inversion (ours)

Figure 10: Visualization results of various inversion process on Imagenet

## D Experimental Details

### D.1 Degradation Operators

**Super Resolution** For super resolution, we use the bicubic downsampling kernel as the degradation operator  $H$ . The weight formula of bicubic interpolation is:

$$w(t) = \begin{cases} \frac{1}{6} ((t+2)^3 - 4(t+1)^3 + 6t^3), & \text{if } |t| \leq 1 \\ -\frac{1}{6} (t^3 - 4(t-1)^3 + 6(t-2)^3), & \text{if } 1 < |t| \leq 2 \\ 0, & \text{otherwise} \end{cases} \quad (37)$$

We calculate the pseudo-inverse  $H^\dagger$  using singular value decomposition(SVD)[15], which can be expressed as follows:

$$H = U\Sigma V^T \quad (38)$$

where  $U$  and  $V$  are orthogonal matrices,  $\Sigma$  is a diagonal matrix, and the elements on  $\Sigma$  are the singular values of  $H$ . Then we can obtain the pseudo-inverse  $H^\dagger$  through:

$$H^\dagger = V\Sigma^\dagger U^T \quad (39)$$

$\Sigma^\dagger$  is the pseudo-inverse of  $\Sigma$ , which can be calculated by taking the reciprocal of non-zero elements on the diagonal of  $\Sigma$ , while keeping the zero elements unchanged.

**Colorization** For colorization, by choosing  $H = [1/3, 1/3, 1/3]$  as a pixel-wise degradation operator, we can convert each pixel from the rgb value  $[r, g, b]^T$  into the grayscale value  $[\frac{r}{3} + \frac{g}{3} + \frac{b}{3}]$ . And the pseudo-inverse is  $H^\dagger = [1, 1, 1]^T$ , which satisfies  $HH^\dagger = I$ .

**Deblurring** For deblurring, we use the gaussian blur kernel as the degradation operator. The gaussian blur kernel can be expressed as:

$$w(i, j) = \frac{1}{2\pi\sigma^2} e^{-\frac{i^2+j^2}{2\sigma^2}} \quad (40)$$

We set the width as  $\sigma = 15.0$  and the kernel size as  $9 \times 9$ . Similar to super resolution, we use SVD to obtain the pseudo-inverse  $H^\dagger$ .

### D.2 Reproducibility Details

**Hyperparameter Settings** Here, we provide the detailed hyperparameter settings of SSD for various inverse problems.

- SSD of 100 NFEs
  - Super-Resolution and Deblurring:
    - \* Inversion step:  $S_{inv} = 15$ ;
    - \* Generation step:  $S_{gen} = 85$ ;
    - \* Shortcut time-step:  $t_0 = 550$ ;
    - \* Proportion of added disturbance:  $\eta = 0.4$
    - \* Steps of attention injection:  $[6, 7, 8, 9, 10, 11, 12, 13, 14]$
  - Colorization
    - \* inversion step:  $S_{inv} = 15$ ;
    - \* generation step:  $S_{gen} = 85$ ;
    - \* Shortcut time-step:  $t_0 = 750$ ;
    - \* Proportion of added disturbance:  $\eta = 0.8$
    - \* Steps of attention injection:  $[6, 7, 8, 9, 10, 11, 12, 13, 14]$
- SSD of 30 NFEs
  - Super-Resolution and Deblurring:
    - \* inversion step:  $S_{inv} = 5$ ;

- \* generation step:  $S_{gen} = 25$ ;
- \* Shortcut time-step:  $t_0 = 550$ ;
- \* Proportion of added disturbance:  $\eta = 0.4$
- \* Steps of attention injection:  $[2, 3, 4]$
- Colorization
  - \* inversion step:  $S_{inv} = 5$ ;
  - \* generation step:  $S_{gen} = 25$ ;
  - \* Shortcut time-step:  $t_0 = 750$ ;
  - \* Proportion of added disturbance:  $\eta = 0.8$
  - \* Steps of attention injection:  $[2, 3, 4]$

**Pretrained models** For CelebA 256×256, we use the denoising network VE-SDE[31, 21], which is pre-trained on CelebA. Pre-trained Model files can be downloaded here provided by SDEdit.

For ImageNet 256×256, we use the denoising network guided-diffusion [7], which is pre-trained on ImageNet. Pre-trained Model files can be downloaded here provided by guided-diffusion.

**Code Availability** We will open-source our code of SSD upon publication to enhance reproducibility.

### D.3 Algorithm

---

#### Algorithm 1 Image Restoration of Distortion Adaptive Inversion

---

**Input:** input measurement image  $y$ , degradation operator  $H$

**Parameters:** inversion step  $S_{inv}$ , generation step  $S_{gen}$ , shortcut time-step  $t_0$ , proportion of added disturbance  $\eta$ , steps of attention injection  $\{S_{attn}\}$

**Output:** restored Image  $x$

---

##### Step 1: Get the Embryo through DA Inversion

- 1:  $x_0 = H^\dagger y$
- 2: Define  $\{\tau_s\}_{s=1}^{S_{inv}}$ , s.t.  $\tau_1 = 0, \tau_{S_{inv}} = t_0$
- 3: Define  $\{\tau_{attn}\} = \{\tau_{s_{attn}}\}$
- 4: **for**  $s = 1, \dots, S_{inv} - 1$  **do**
- 5:   **if**  $\tau_s \in \{\tau_{attn}\}$  **then** ▷ Restore Attention Map
- 6:      $\epsilon \leftarrow \epsilon_\theta(x_{\tau_s}, \tau_s, \emptyset)$ ;
- 7:   **else**
- 8:      $M_{\tau_s}^l, \epsilon \leftarrow \epsilon_\theta(x_{\tau_s}, \tau_s, \emptyset)$ ;
- 9:   **end if**
- 10:  $x_{0|\tau_s} \leftarrow f_\theta(x_{\tau_s}, \tau_s)$ ;
- 11:  $z \sim \mathcal{N}(0, 1)$
- 12:  $x_{\tau_{s+1}} = \sqrt{\alpha_{\tau_{s+1}}}x_{0|\tau_s} + \sqrt{1 - \alpha_{\tau_{s+1}} - \eta\beta_{\tau_{s+1}}}\epsilon + \sqrt{\eta\beta_{\tau_{s+1}}}z$  ▷ DA Inversion
- 13: **end for**
- 14:

##### Step 2: Get HQ Image from the Embryo

- 15: Define  $\{\tau_s\}_{s=1}^{S_{gen}}$ , s.t.  $\tau_1 = 0, \tau_{S_{gen}} = t_0$
  - 16: **for**  $s = S_{gen}, \dots, 2$  **do**
  - 17:   **if**  $\tau_s \in \{\tau_{attn}\}$  **then** ▷ Attention Map Injection
  - 18:      $\epsilon \leftarrow \epsilon_\theta(x_{\tau_s}, \tau_s, M_{\tau_s}^l)$
  - 19:   **else**
  - 20:      $\epsilon \leftarrow \epsilon_\theta(x_{\tau_s}, \tau_s, \emptyset)$ ;
  - 21:   **end if**
  - 22:  $x_{0|\tau_s} \leftarrow f_\theta(x_{\tau_s}, \tau_s)$  ▷ Denoising Step
  - 23:  $\hat{x}_{0|\tau_s} \leftarrow (I - H^\dagger H)x_{0|\tau_s} + H^\dagger y$  ▷ Back Projection Step
  - 24:  $x_{\tau_{s-1}} = \sqrt{\alpha_{\tau_{s-1}}}x_{0|\tau_s} + \sqrt{1 - \alpha_{\tau_{s-1}} - \sigma^2}\epsilon + \sigma z$
  - 25: **end for**
  - 26: **return**  $x_0$
-

## E Time and Memory Consumption

In our main paper, we use neural function evaluations(NFEs) as the metrics of sampling speed. Here we further measure the time consumption and memory consumption of different methods when restoring a single image. The results are illustrated in Tab. 3. We conduct super-resolution 4× experiments using a single Nvidia RTX 3090 GPU.

It is observed that the projection-based methods, including DDRM[15], DDNM[36], and our SSD, exhibit comparable time consumption(0.06 s/it for celeba[13], 0.11 s/it for imagenet[6]) and memory consumption. The discrepancies in consumption mainly stem from variations in implementation details of their code. On the other hand, the gradient-based methods such as DPS[3] require additional time and memory consumption, primarily due to the inclusion of back-propagation operations for gradient calculations at each steps.

Method	Celeba [13]			Imagenet [6]		
	NFEs	Time(s/image)	Memory(MB)	NFEs	Time(s/image)	Memory(MB)
DDRM-30 [15]	30	1.57	4551	30	3.02	6227
DDRM-100 [15]	100	5.14	4551	100	10.34	6227
DPS [3]	100	12.70	5339	100	36.87	9583
DDNM [36]	100	4.98	4539	100	10.11	6215
SSD-30	30	1.78	2765	100	3.64	5955
SSD-100	100	6.08	2765	100	11.98	5955

Table 3: Comparisons on Time Consumption and Memory Consumption of different methods.

## F Further Ablation Studies

In the main text, we have already examined the impact of  $(t_0, \eta)$  on the performance of applying DA Inversion only. Here we extend our discussion to explore the impact of  $(t_0, \eta)$  on the performance of SSD (DA Inversion + consistency constraints). To identify the most suitable combination, we perform experiments with different  $(t_0, \eta)$  values for the super resolution 4× task on Celeba datasets. Results are presented in Tab. 4.

$\eta$	$t_0$	PSNR ( $\uparrow$ )	FID ( $\downarrow$ )	LPIPS ( $\downarrow$ )	$\eta$	$t_0$	PSNR ( $\uparrow$ )	FID ( $\downarrow$ )	LPIPS ( $\downarrow$ )
0.1	550	27.12	39.12	0.253	0.4	450	27.17	39.35	0.253
0.4	550	27.13	38.24	0.252	0.4	550	27.13	38.24	0.252
0.7	550	27.15	38.63	0.252	0.4	650	27.10	38.70	0.252
1.0	550	27.15	38.80	0.252	0.4	800	27.06	38.90	0.253

(a) Performance with different  $\eta$ .

(b) Performance with different  $t_0$ .

Table 4: Ablation studies on  $\eta$  and  $t_0$ .

Furthermore, we perform ablation studies to validate the effectiveness of the proposed modules in SSD. As depicted in Fig. 11 and Tab. 5, applying DDIM Inversion alone leads to faithful but unrealistic results, whereas applying DA Inversion alone produces faithful and realistic results. Moreover, the integration of consistency constraints in SSD, including back projection and attention injection, further improves the performance.

Method	PSNR ( $\uparrow$ )	SSIM ( $\uparrow$ )	FID ( $\downarrow$ )	LPIPS ( $\downarrow$ )
<b>DDIM Inversion alone</b>	18.24	0.448	107.04	0.558
<b>DA Inversion alone</b>	23.54	0.663	41.53	0.321
<b>SSD</b>	28.74	0.816	32.45	0.202

Table 5: Quantitative evaluation for ablation study.

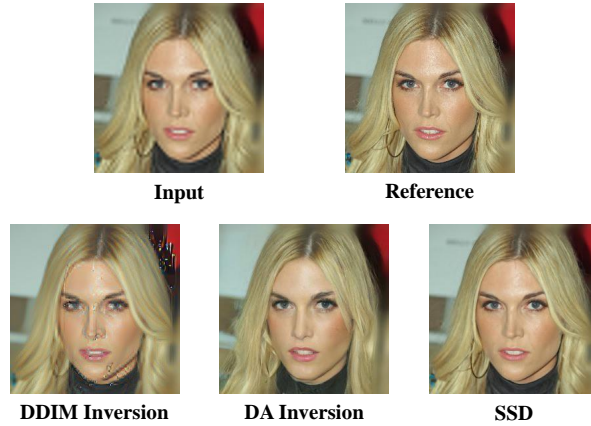


Figure 11: Visual comparison for ablation study. Performing DDIM Inversion leads to faithful but unrealistic results, while performing DA Inversion only produces faithful and realistic results. And SSD with additional consistency constraints during the generation process generates best results

## G Generative process of the proposed method

- a) DA Inversion only;
- b) DA Inversion +

We provide restoration results of SSD on SR tasks at various scales (ranging from  $2\times$  to  $32\times$ ) using an average-pooling downsampler, as depicted in Fig. 12. These results demonstrate the ability of SSD to handle diverse degrees of degradation. Additionally, We present more qualitative results and comparisons for various IR tasks and datasets, as illustrated in Fig. 13, 14, 14, 15, 16, 17.

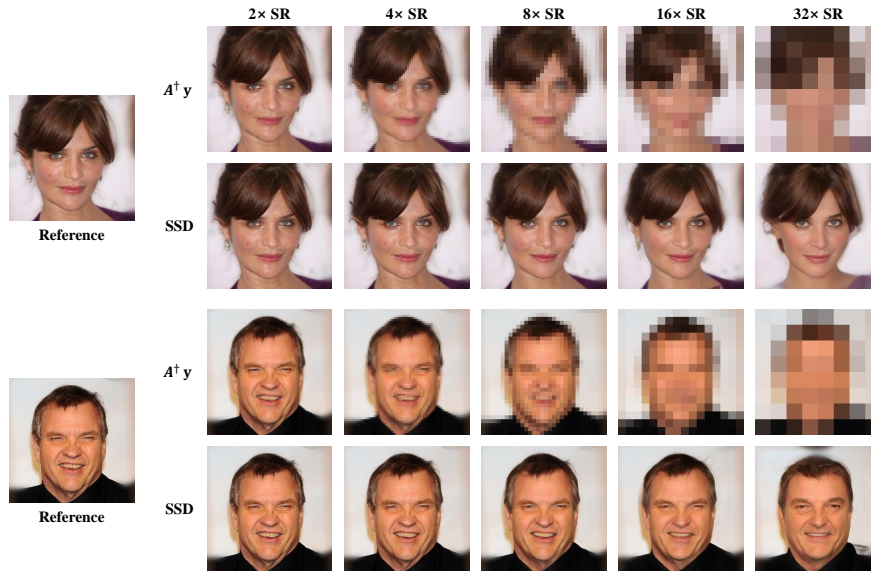


Figure 12: Restoration results at different average-pooling downsampling scales on Celeba Dataset



Figure 13: Image restoration results of SSD On CelebA Dataset

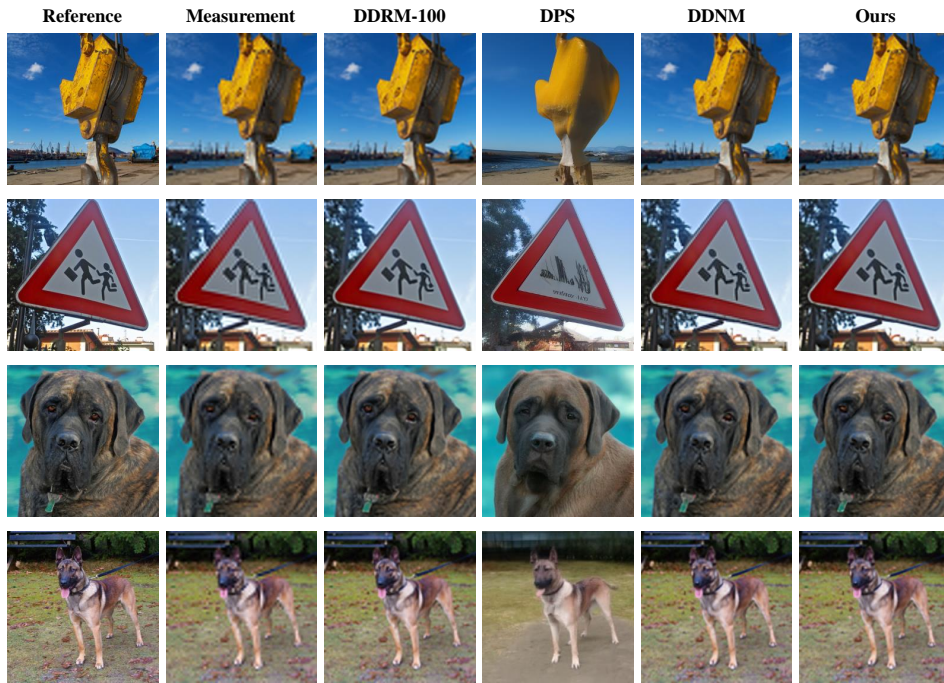


Figure 14: Comparison of results on  $4\times$  super-resolution task using different zero-shot IR methods on the Imagenet dataset

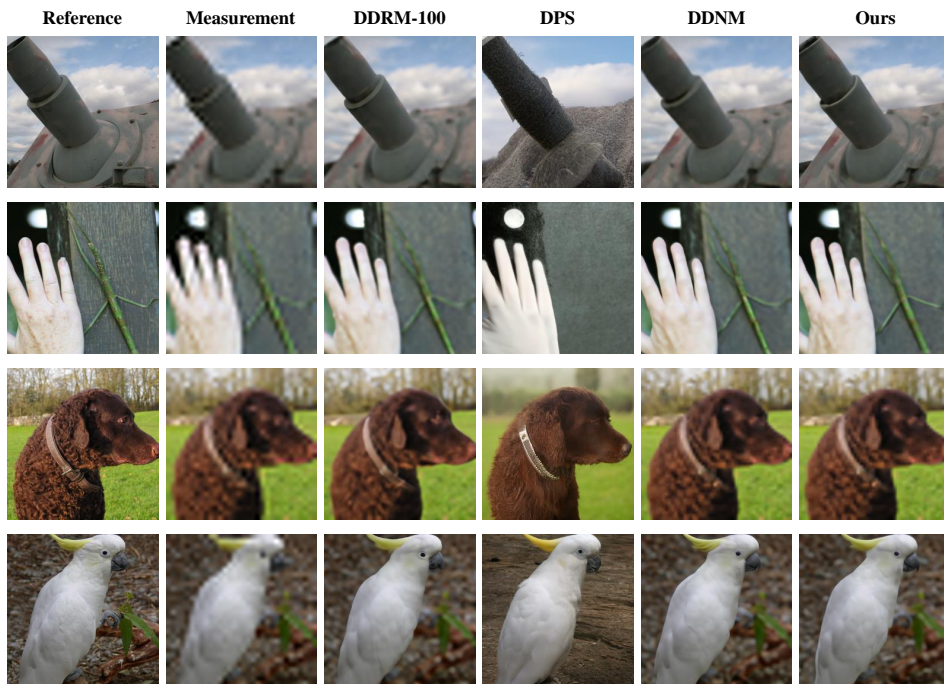


Figure 15: Comparison of results on  $8\times$  super-resolution task using different zero-shot IR methods on the Imagenet dataset



Figure 16: Comparison of results on colorization task using different zero-shot IR methods on the Imagenet dataset

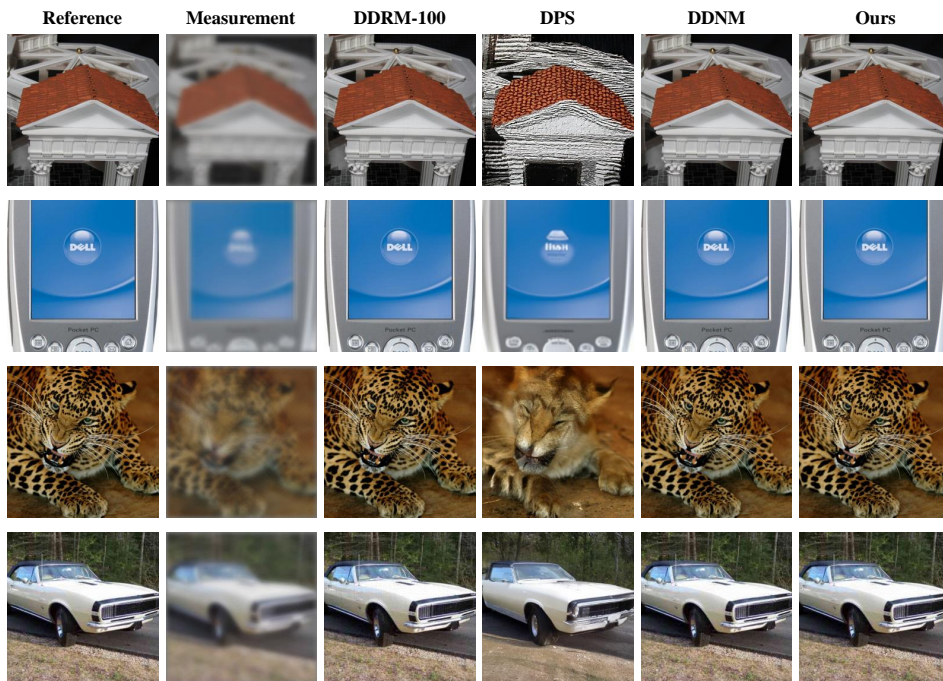


Figure 17: Comparison of results on deblurring task using different zero-shot IR methods on the Imagenet dataset